Thermal and Dielectric Properties from the Chang'E 2 Microwave Radiometer

Contents

1 Scientific/Technical/Management

1.1 Objectives and Expected Significance

The primary objective of this study is to produce a quantitative model for the interpretation of the Chang'E-2 Microwave Radiometer (MRM) data. The microwave brightness temperature of an object is directly related its physical temperature and its dielectric properties. Using LRO Diviner-constrained subsurface temperature models and MRM measured brightness temperature, we will constrain ilmenite composition, rock abundance, and geothermal heat flux. We will also provide archival and simple error corrections of this data for broader use in the planetary community.

1.1.1 Passive microwave and subsurface temperatures

In this proposal, we detail how the Chang'E-2 (CE-2) microwave radiometer (MRM) data, when combined with the Lunar Reconnaissance Orbiter Diviner thermal infrared data and models, will be used to reconstruct subsurface temperatures and global dielectric properties of the Moon. We will use thermal and radiative transfer models along with CE-2 and LRO diviner data to derive global estimates of the dielectric, thermal, heat flow and density properties of the lunar regolith. **This is a unique data set in a new frequency range that is absent from NASA's lunar reconnaissance**, providing a novel view of the lunar surface (e.g. **Figure 1** and **2**). This dataset has been underutilized due to lack of underlying theory in its interpretation and calibration issues which we show are correctable. **We expand here on preliminary research (e.g. Feng et al., 2020; Siegler et al, 2020) which uses these measurements to reconstruct regolith thermal and dielectric properties, rock abundance, and geothermal heat flow.** This data set shows huge promise to open up many new avenues of research, greatly enhance the data set from other lunar missions, and inform the design of future instrumentation.

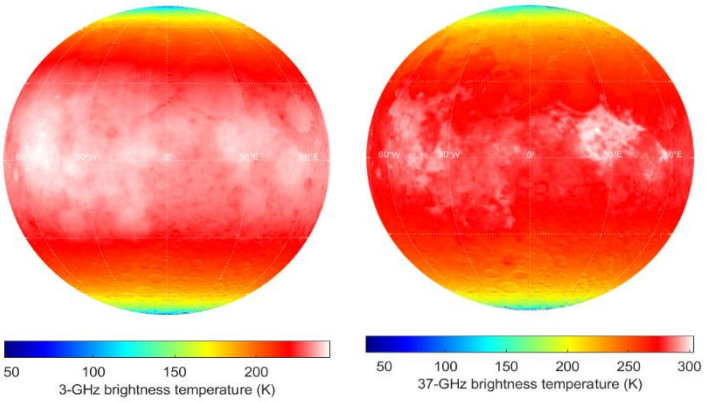

Figure 1: Lunar near-side brightness temperature from CE-2 MRM 3- and 37-GHz frequencies at "noon" (data from 12:30 to 14:30 are used for this figure) to show the high quality of data available. Note the appearance of high-titanium mare (such as mare Tranquillitatis) as hotter, which results from shallower, warmer, emissions.

The first high resolution global lunar microwave frequency maps were made by the Chang'E-1 (CE-1) and Chang'E-2 (CE-2) missions (Wang et al., 2010; Zheng et al., 2019). The MRM carried by the CE-2 mission in 2010-2011 measured the brightness temperature (T_B) of the Moon at frequencies of 3, 7.8, 19.35 and 37 GHz. This instrument is a copy of CE-1 MRM but with higher resolution due to CE-2's lower altitude orbit. Also, CE-2 MRM undertook a better ground test than CE-1 MRM (Feng et al., 2013). During its 7 months of operation in lunar orbit, CE-2 MRM obtained about 8.7 million measurements. The dataset has a spatial resolution of approximately 25 km at 3 GHz and 17.5 km at 7.8, 19.35 and 37 GHz. The time interval between each record is 1.6 s, during which the satellite flew about 2.6 km, leading to a high overlapping

ratio along the track. All of the T_B data are archived in 2401 files (one for each orbit) according to the PDS3 Data Standards. These files are published by Data Release and Information Service System of China's Lunar Exploration Program (http://moon.bao.ac.cn/index_en.jsp). These measurements have been used to reconstruct regolith thickness (Fa & Jin, 2010), dielectric properties (Feng et al., 2020; Gong et al., 2014), subsurface temperatures (Hu et al., 2017), and geothermal heat flow (e.g. Siegler and Feng, 2017).

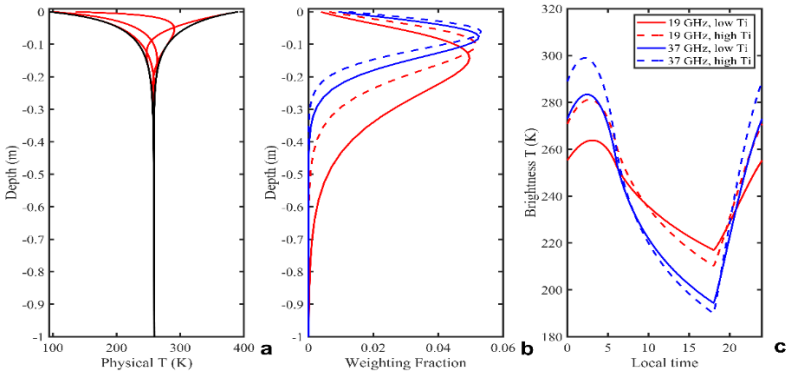

Figure 2: (a) Physical temperature (model) of the lunar subsurface (b) weighting functions (depth over which microwave emission comes) for 19 and 37 GHz emission with high and low titanium (c) the resulting diurnal microwave brightness temperature (T_B) variations.

The Diviner Lunar Radiometer Experiment (Diviner), currently orbiting the Moon onboard LRO, is a 9-channel visible and infrared radiometer measuring the spectral brightness temperature at 7 mid- to far-infrared wavelengths (Paige et al., 2010). Diviner's infrared channels have an effective resolution of ~160 by 320 m on the lunar surface. It has been systematically mapping the Moon since July 5, 2009 at solar (0.3 - 3μm) and infrared (7.8 - 400μm) wavelengths covering a full range of latitudes, longitudes, local times and seasons (Williams et al., 2017, 2019). Thermal properties of the lunar regolith have been studied by several researchers using Diviner (e.g. Bandfield et al., 2011, 2015; Feng et al., 2020; Hayne et al., 2017; Vasavada et al., 2012). PI Siegler, Science PI Feng, and Collaborator Hayne are all funded for their Diviner work and are not requesting funding for those efforts here- this proposed effort is primarily to allow Dr. Feng to directly apply his Diviner experience to the Chang'E MRM data, which we believe will greatly enhance the return from both instruments.

These two datasets are complementary, yet intertwined. The physical temperature constrained by Diviner will allow us to interpret the brightness temperatures (T_B) measured by CE-2 MRM. As illustrated in **Figure 2**, Diviner-constrained models of the subsurface temperature (**Figure 2a**) are combined with a model of the "weighting function" (which determines the depth from which microwave wavelength thermal emissions will come, detailed in Section 1.2.1). This allows for a retrieval of microwave brightness temperature (plotted against time in **Figure 2c**). These brightness temperatures depend on the depth from which the radiation is emitted, which in turn depends dominantly on frequency (37 GHz in blue, 19 GHz in red), ilmenite content (0% in solid line, 8% in dashed line), density (which is assumed not to change in the figures in this proposal) and changes in physical temperature (such as additional geothermal heat that is not in the initial physical temperature model). **Therefore, with a detailed thermal model constrained by Diviner infrared observations, we can use CE-2 MRM observations to determine the effect of variations in ilmenite (Task 1), rock fraction/density (Task 2), and heat flux (Task 4).**

We will use our experience with the LRO Diviner data (again-Siegler, Feng, and Collaborator Hayne are all Diviner team members) and Diviner-based models to enable processing and interpretation of the Chang'E microwave data. The ground stages of this work have been recently published (Feng et al., 2020), submitted (Siegler et al., 2020, JGR in review) and presented at several LPSC and AGU meetings (Siegler et al. 2017, 2018, 2019…).

From our observations and experience with the MRM data, we make several first-order observations and assumptions that lead to our 4 proposed tasks:

1) Ilmenite is the predominant cause for changes in the microwave diurnal T_B amplitude and this data can fill a gap in low ilmenite characterization.

2) That the presence of rocks explains most of the remaining large amplitude features in the microwave T_B data and that this data can provide new constraints on rock distribution filling a gap in mapping <30cm, not clearly identified in Diviner rock abundance.

3) That there is a calibration issue with the 3.0 and 7.8 GHz channel, but these can be addressed in part with our model results.

4) The lowest frequency data is sensitive to deep temperatures (>1m) and may see variations due to regional changes in geothermal heat flow.

To address these open assumptions will divide this new project into 4 clear tasks:

Task 1: We will produce global maps and models of the loss tangent due to the presence of ilmenite. Diurnal T_B amplitudes are proportionate to physical temperature amplitudes (constrained by Diviner) and dielectric loss. Some minerals, such as ilmenite have large dielectric loss, causing them to greatly affect microwave amplitudes.

Task 2: Once a trustworthy characterization of ilmenite's impact on the loss tangent has been obtained, we will produce global maps and models of the loss tangent due to the presence of surface and sub-surface rocks. Density changes from rocks and ice will also affect T_B amplitudes. We will map changes in amplitude (and therefore dielectric loss) to look for anomalous regions that could imply the existence of rocks. As microwave emissions come from depth (up to ~3-5m for 3 GHz), this should allow for profiles of depth dependence of these dielectric anomalies.

Task 3: Data processing and re-calibration of known (Feng et al., 2020) absolute value and "terminator" errors in the 3 and 7.8 Ghz data based on our model results. This recalibration will be based both on available spacecraft system measurements (not all are available) and by direct comparison with model results from Tasks 1 and 2. This task will also cover the archiving of both the original Chang'E dataset (not on PDS) and our recalibration. This task is critical for allowing work in:

Task 4: Constraint of geothermal heat flux from MRM data. In low-loss regions of the Moon, the lowest of the MRM frequencies (3 GHz and feasible 7.8 GHz) is receiving a substantial amount of heat from layers below the reaches of diurnal surface temperature variations. Therefore, changes in T_B may be due to variations in local geothermal heating. In the polar shadowed regions, an apparent low density and low thermal conductivity lead it to be feasible to constrain geothermal heat with all MRM channels. While this task lies at the "furthest reaches" of the MRM data, preliminary work shows promise that some heat flow constraints can be made with the current data.

1.2 Technical Approach and Methodology

1.2.1 Current work: Existing models to interpret microwave data

Microwave brightness temperature (T_B) is effectively the integrated physical temperature of a material over a given depth weighted by the dielectric loss of that material. It is related to physical temperature by $T_B = \int_0^\infty T(z)\, w(z) dz$, where *T(z)* is the temperature profile and *w(z)* is the microwave weighting function. The weighting function characterizes depths from which radiation

emitted in the microwave arises. It is determined by frequency, dielectric loss and density of the medium. Dielectric loss quantifies a dielectric material's inherent dissipation of electromagnetic energy. It can be parameterized in terms of either the loss angle δ or the corresponding loss tangent tan δ.

To interpret the microwave data and study the thermal and dielectric properties of the lunar regolith, we are developing a theoretical model including these geophysical parameters to fit MRM data. Also, this model needs to meet the regolith's surface temperature constrained by Diviner. **Our method consists of two parts: (1) a one-dimensional thermal model and (2) a microwave radiative transfer model.**

The one-dimensional numerical thermal model is widely used to interpret lunar surface temperature data (e.g. Hayne et al., 2017). This finite-difference approach is robust and extensively validated, with heritage from diverse areas of planetary science (e.g. Keihm & Langseth, 1973; Kieffer, 2013; Paige, 1992; Vasavada et al., 1999). Recently, Hayne et al. (2017) mapped thermal inertia of the Moon's global regolith fines layer by fitting the thermal models to nighttime temperature of fines layer. The time- and depth-dependent subsurface temperatures can be calculated by solving the one-dimensional heat diffusion equation (e.g. Hayne et al., 2017; Vasavada et al., 1999, 2012):

$$\rho(z)C(z,T)\frac{\partial T(z,t)}{\partial t} = \frac{\partial}{\partial z}\left(k(z,T)\frac{\partial T(z,t)}{\partial z}\right), \qquad (1)$$

where $T(z, t)$ is subsurface temperature at a given depth, z (cm), and local time, t (s). ρ is regolith density (kg/m^3), C is specific heat (Jkg^{-1}K^{-1}), and k is thermal conductivity (Wm^{-1}K^{-1}).

Once the subsurface temperature is derived, the T_B of lunar regolith can be simulated by a 1-D radiative transfer model originated from Ulaby et al. (1981) incoherent method. The depth, thickness, density, and temperature of each regolith layer which are outputs of thermal model are used to calculate T_B emitted by lunar regolith at microwave frequencies. In a one-dimensional situation, with nadir viewing angle, the T_B of a non-scattering medium can be written as:

$$T_B(v,t) = \int_0^\infty T(z,t)\,w(z,v)dz = (1-\Gamma)\int_0^\infty T(z,t)\,\kappa_\alpha(z,v)e^{-\tau(0,z)}dz, \qquad (2)$$

where $T(z, t)$ is subsurface temperature profile solved in equation (1). $w(z, v)$ is weighting function at a frequency of v. κ_α is power absorption coefficient in the form of $\kappa_\alpha = 2\frac{2\pi v}{c}\left(\frac{\varepsilon}{2}\left(\sqrt{1+tan^2\delta}-1\right)\right)^{1/2}$. ε is dielectric permittivity and $tan\delta$ is dielectric loss tangent of the medium. $\tau(0, z)$ is optical depth defined by $\tau(0, z) = \int_0^z \kappa_\alpha(z', v)dz'$. Γ is the reflectivity at the boundary which can be calculated from ε. **Figure 3** shows an example weighting function computed from equation (2).

With the 1-D thermal model described by equation (1) and the microwave radiative model described by equation (2), we reconciled the data from the LRO Diviner infrared radiometer and CE-2 MRM in lunar highlands. Based on this work (Feng et al., 2020), a new incidence angle dependent bolometric Bond albedo of lunar surface is proposed. The existing regolith thermal conductivity models (Hayne et al., 2017) have also

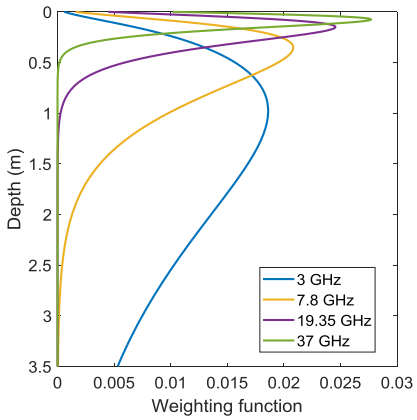

Figure 3: Weighting function at each frequency in regolith of lunar highlands (following Feng et al., 2020).

been updated. Additionally, we found the dielectric loss tangent of the regolith in lunar highland is much larger than previous studies, which was based on laboratory measurements of Apollo samples mostly at 1 MHz and 450 MHz (Carrier et al., 1991). To match the diurnal variation of T_B measured by CE-2 MRM, we propose a new loss tangent equation for highland regolith over the MRM frequency range as:

$$\tan\delta = 10^{(0.312\rho+0.0043f-2.64)} \quad (3)$$

where f is the frequency with a unit of GHz, and ρ is density. By using this loss tangent model, our model fit the MRM high-frequency data well in highlands globally (**Figure 4 and 11**). **Figure 11**, which is placed later for its relevance to Task 3, shows that this model matches amplitude measurements at 3.0 and 7.8 GHz well, despite an apparent absolute value offset. **Figure 4** also illustrates what is meant by "diurnal microwave amplitude" which we fit later in the proposal.

Our previous work (Feng et al., 2020; Siegler et al., 2020- submitted) has created a promising framework and applied it to highland regolith. In this proposed effort, we will modify current models to conduct analysis on regolith Titanium (Ti) composition, rock abundance and geothermal heat flux.

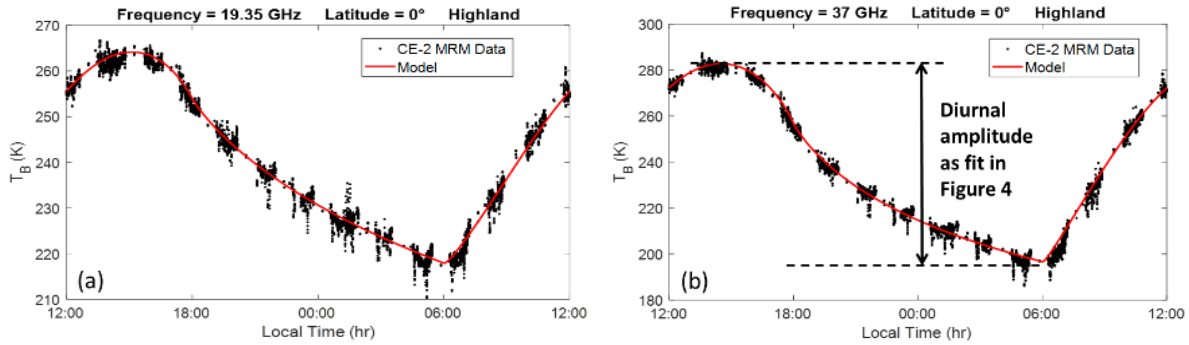

Figure 4: Our current model fit the MRM data in highlands at lunar equator at 19.35 and 37 GHz.

1.2.2 Task 1: The content of titanium-rich ilmenite in lunar regolith

TiO_2 has been mapped on the Moon using Clementie (Lucey et al., 2000) and LROC (Sato et al., 2017) data. However, this data cannot be uniquely interpreted as ilmenite and has not been constrained for fractions below 2%. Microwave data is uniquely sensitive to ilmenite (e.g. Sohn et al., 1994) and will not be affected by pyroxene minerology below 2% like the spectral data, filling a gap in the knowledge of ilmenite distribution on the Moon.

This work, which looks at diurnal amplitudes, does not depend on the recalibration efforts discussed in Task 3, but will inform model guidelines for the suggested recalibration. Essentially, these models will be designed to match data amplitudes (which are well-calibrated) and predict absolute temperature values for the data (which are poorly calibrated) to which we believe the data should be adjusted to make a complete, physically consistent interpretation of the data.

As the diurnal amplitude of T_B is directly proportional to loss tangent, the loss tangent of specific location can be determined by its diurnal T_B amplitude. The ability to constrain the loss tangent of the lunar regolith allows for new constraints on the composition and density of the lunar surface. Ilmenite is known to have a high loss tangent (e.g. Montopoli et al., 2011; Sohn et al., 1994), explaining the strong correlation with high-titanium mare (Lucey et al., 2000; Sato et al., 2017), especially in Mare Tranquillitatis and Oceanus Procellarum.

To begin this task, we will map microwave amplitudes to examine the effect of ilmenite on the loss tangent. To maximize the resolution of a map of the diurnal microwave amplitudes, we divide the Moon into ¼ degree (~7.6 km) bins. Due to the spatial resolution and relatively sparse diurnal coverage of the CE-2 mission, each bin is filled with an average of the ½ degree (~15.2 km) square around this bin (to ensure each bin contains at least 20 unique times of day). This provides an approximate match to the nominal MRM 17.5-25 km footprint while maximizing the resolution of the map.

Figure 5 shows the resulting scaled diurnal brightness temperature amplitude found for each frequency. Here we point out that despite the absolute calibration issues apparent in the 3.0 and 7.8 GHz channels (detailed in Task 3), the diurnal amplitude maps clearly show that this information is above the noise level of the instrument. This confirms that the measurement repeatability of the CE-2 MRM is good, even if absolute calibration has issues. These amplitudes have been normalized to those at the lunar equator by fitting the latitudinal trend for an area of highlands (choosing the relatively featureless area between 12.5˚and 62.5˚longitude) and remove it from the amplitude maps.

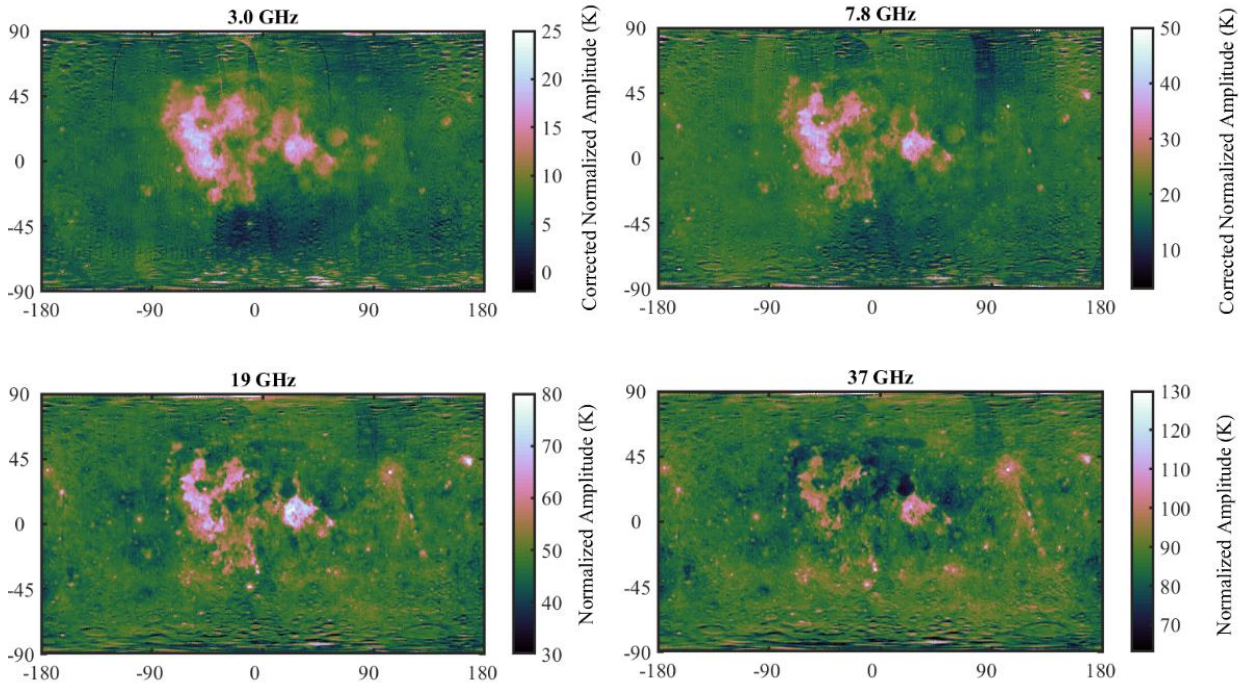

Figure 5. Global brightness temperature amplitudes at all Chang'E frequencies after a time of day correction and latitudinal normalization (From Siegler et al., 2020).

These maps reveal a wealth of information about microwave loss variations on the lunar surface. Clearly, as we will go into detail later, different frequencies are sensitive to different materials, potentially varying with depth, and rock size distributions. As was also seen in the amplitude maps, most notable features are the correlations with titanium as mapped by spectral techniques in Lucey et al. (2000) and Sato et al. (2017) seen in **Figure 6** and global rock distribution mapped by thermal infrared in Bandfield et al. (2011, **Fig. 8b**).

The large amplitude areas are highly consistent with the location where TiO_2 abundance is larger than 2%, which implies a feasibility that the TiO_2 abundance could be inferred from diurnal

T_B amplitude. The TiO_2 affects the loss tangent ($\tan\delta$) of lunar regolith in the form of a widely used equation (Carrier et al., 1991):

$$\tan\delta = 10^{(0.038S+0.312\rho-3.26)} \qquad (4)$$

where S is weight percent of TiO_2+FeO (primarily in the form of ilmenite (Sohn et al., 1994)), ρ is density of regolith. Recently, Boivin et al. (2019) also made Systematic measurements of the complex relative permittivity of powdered bytownite (a Ca-rich plagioclase feldspar) mixed with increasing amounts of ilmenite. These measurements will help us estimate the ilmenite once the loss tangent of a specific location is known.

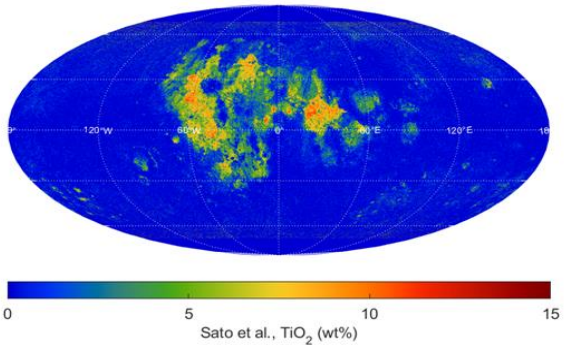

Figure 6. Global map of lunar TiO_2 abundance derived from spectral techniques (Sato et al., 2017).

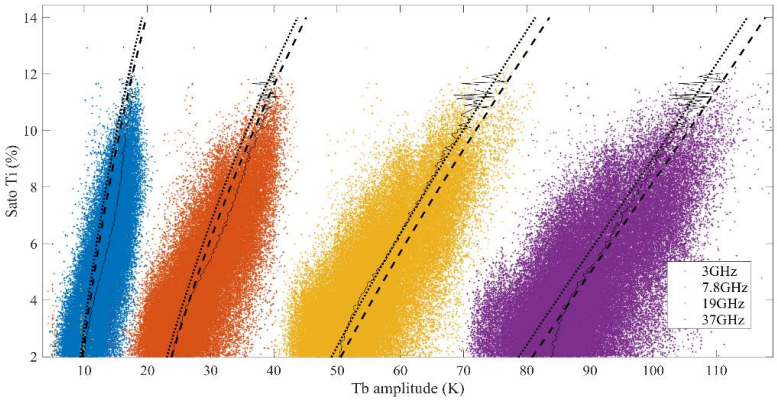

Figure 7: Diurnal Tb Amplitudes vs LROC derived Ti (Sato et al., 2017) for the four Chang'e 2 MRM channels.

Using these data, we will produce a global microwave-derived map of ilmenite. This has the potential to fill in current gaps in the LROC team's spectrally-derived ilmenite (Sato et al., 2017) which are not sensitive to ilmenite contents below ~2%. Below ~2% pyroxene begins to dominate the band ratio they use to derive ilmenite. We will use the correlation between T_B amplitude and LROC derived Ti (**Figure 7**) to drive a relationship between amplitude and ilmenite that can be used even for small ilmenite content. We will also work with existing laboratory data (e.g. Bovin et al, 2019) to develop a consistent relationship between laboratory and lunar-derived ilmenite and the loss tangent.

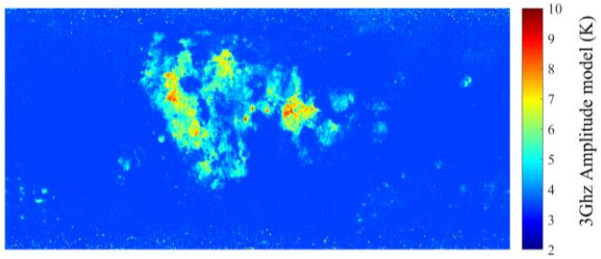

Figure 8. Fits from Fig. 7 is used to make a forward model of Tb amplitude from LROC Ti data alone.

This work will be led by Science PI Feng and PI Siegler. We expect their efforts (0.5 FTE and 0.08 FTE) will be divided roughly equally between model fitting of data and working with the processing of the data itself.

1.2.3 Task 2: Rock abundance constrained by microwave data

In this proposed work, we will use the titanium maps from Task 1 to remove all the amplitude/loss tangent affects from ilmenite. The remaining feature affecting the amplitude

should be the presence of rocks. As different size rocks affect each wavelength, we will compare these residual amplitudes with models of size-dependent rock abundance derived from LRO Diviner (e.g. Elder et al., 2016). We will use the wavelength dependence of the microwave amplitude to constrain the scale of rocks which are present on the lunar surface.

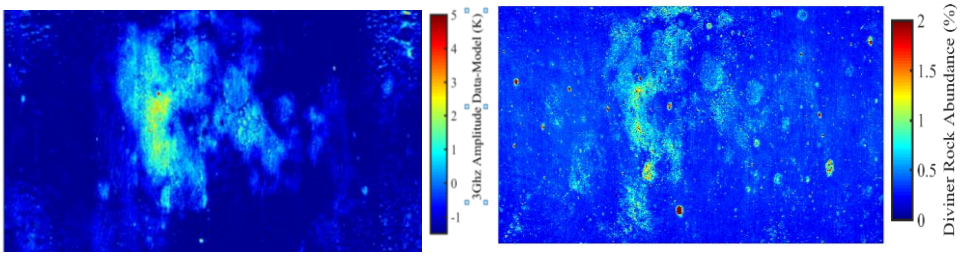

Figure 9: (a) the 3 Ghz data with the influence of the loss tangent removed (data minus our 3 Ghz model, Fig. 7). Features result from shallow/surface rock populations, ~10-100cm in diameter, and (b) LRO Diviner rock abundance.

As seen in **Figure 5**, the low-titanium, rock-poor highlands show fairly uniform amplitude. High amplitude regions in the highlands nearly universally map to rocky impact craters, with most surrounded by a relatively low-loss halo at lower frequencies. Using the results from Task 1, we can also characterize rocky ejecta in high-Ti mare areas. Drawing from the low-Ti highlands, we will be able to use models for the effect of rocks to aid in further differentiating ilmenite and rocks.

As seen in preliminary mapping (e.g. Figure 5), high frequency data show a stronger correlation with distal ejecta and rays, such as those around Giordano Bruno (GB). The GB rays do not appear in the Diviner rock abundance, but are seen in Diviner regolith thermal inertia (**Fig. 10b**, from Hayne et al., 2017), implying that these are areas dominated by small rocks, which have been categorized as high thermal inertia regolith. Interestingly, this ejecta nearly vanishes in the 3.0 and 7.8 GHz data, save for small high values at the crater itself and along the large, south-east trending ray. This is likely related to the size distribution of the rocks within the ejecta rays. High frequencies will not penetrate small, cm-scale rocks, but low frequencies will pass through them, much as cell phone signals pass through walls. Large rocks will block all frequencies. This hints that multi-frequency microwave data may provide a potential means of determining the average rock grain size distribution. Multi-frequency microwave examination of these areas may provide further insight on the size fraction within ejecta.

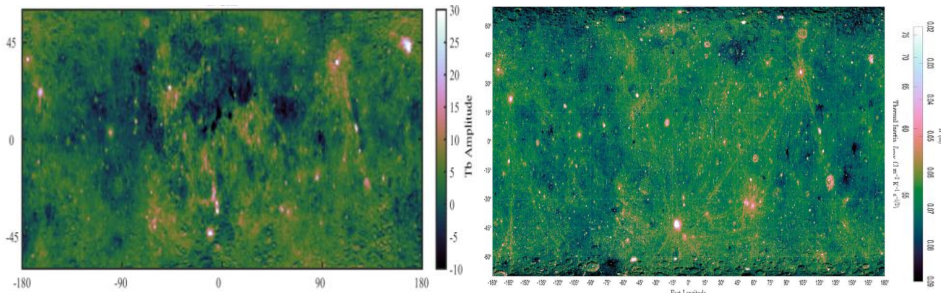

Figure 10: (a) the 19 Ghz data minus our 19 Ghz forward model). Features result from shallow/ surface rock populations, <10cm in diameter, resembling (b) LRO Diviner Regolith thermal inertia, which is influenced by small rocks (Hayne et al.,

With the fitting curve shown in **Fig. 7**, we can now create a full forward model of expected diurnal amplitude at any given frequency if Ti variations were the only variable affecting T_B. **Figure 8** is an example of a map of expected 3GHz amplitude from Ti (Sato et al., 2017) alone. If we simply take the forward model from **Fig. 8** and difference it from the data (**Fig. 5a**), we

should be able to produce a map of all non-Ti derived amplitude changes, shown for 3 GHz in **Fig. 9a**, which bears a clear spatial resemblance to surface rock abundance as derived by the LRO Diviner infrared radiometer (**Fig. 9b**). Higher frequencies would reveal smaller rocks as illustrated in **Figure 10**, which compares the 19 Ghz "difference map" (**Fig. 10a**) to Diviner regolith thermal inertia (**Fig. 10b**), which is sensitive to small rocks (Hayne *et al*., 2017). This shows that different frequencies will be sensitive to different size/depth rocks.

The disappearance of rays between 19 GHz (1.6 cm wavelength) and 7.8 GHz (3.8 cm wavelength, see **Fig. 5**) implies that rocks in the Giordano Bruno ejecta are mainly less than 2-3 cm in diameter, too small to be observed in Diviner rock abundance (Bandfield et al., 2011). Many other highlands craters appear bright at their center at all frequencies, implying large rocks. Many of these craters have bright, high amplitude, ejecta blankets at high frequency, but these become low amplitude at low frequencies. Using the frequency dependence of the microwave amplitude, we will constrain the approximate length scale of rocks/pebbles that are present. This work will also be led by Science PI Feng and PI Siegler. We expect their efforts (0.5 FTE and 0.08 FTE) will be divided roughly equally between model fitting of data and working with the processing of the data itself.

1.2.4 Task 3: Data correction and archiving

For Tasks 1 and 2, characterization of the microwave amplitude was all that was necessary. As we have shown (here and in Feng et al., 2020; Siegler et al., 2020 in review), the CE-2 microwave amplitudes appear to be well-calibrated. However, this is not the case for the absolute value of the 3 and 7.8 GHz channels. We find that our preliminary loss tangent model (consistent with Diviner and the MRM 19.35 and 37 GHz, **Figure 4**) predicts much higher (~12 and 18 K hotter) temperatures than seen in the 3- and 7.8-GHz data (**Figure 11**). In addition to the general offset from expectations, we noted that the largest difference appears at around 6am and 6pm local time, which when the spacecraft approached the lunar terminator.

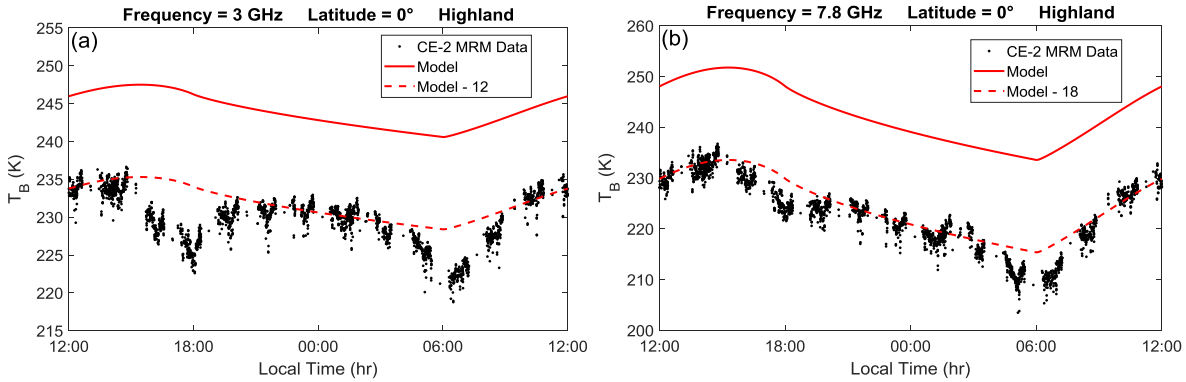

Figure 11. MRM data and proposed theoretical model at (a) 3 GHz and (b) 7.8 GHz.

The CE-2 MRM instrument is calibrated using a second set of space-looking cold horns, orthogonal to cold, 2.7 K space (though the 3.0 GHz cold horn antenna was canted and extra 15˚ from orthogonal in to avoid an error in CE-1, in which the calibration horn observed part of the Moon (Feng et al., 2013)). It is believed that the absolute offset (18K and 12K from our 7.8 and 3 GHz models, respectively) is most likely caused by a contamination of the calibration horns by the warm lunar surface (Hu et al., 2017). These models can be used to characterize likely

subsystem temperatures where they are unavailable. Where system temperatures are unavailable in accessible Chinese archives, they need to be re-derived based on reverse engineered data.

For instance, the 6 am/pm local time error seems well informed by the difference observed from our model predictions. As can be seen in **Figure 12**, the difference from the expected model shape peaks as the spacecraft approach and departed the terminator. As the Chang'E-2 spacecraft solar panels had only a single axis gimbal, a reorientation of the spacecraft in this precise manner was required to maintain their orientation with respect to the Sun (**Figure 12**). This make the MRM calibration horns, which normally looked in the forward-track direction, to point perpendicular to the motion of the spacecraft. In this orientation, this unfortunately meant that the cold horn antenna, especially the relatively large beamwidth 3.0 and 7.8 GHz channels, to point towards the Sun. Facing the Sun brought more direct illumination which appears to have heated the large 3.0 and 7.8 GHz cold horns and lead to a lower calibrated T_B on the Moon. We can model the system temperature change as a function of existing data (such as spacecraft pointing) to characterize these issues and determine the most reliable way to reduce the data. All changes we make to the original data will be fully documented and be reversible, allowing for future users to remove any assumptions made in our recalibration pipeline.

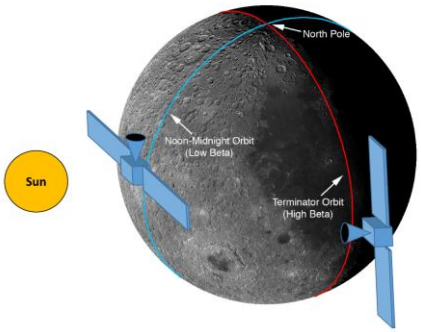

Figure 12: Geometry of the Chang'E 2 spacecraft during noon-midnight and terminator orbits. Terminator orbits lead to continuous illumination of the spacecraft, which we deem the cause of the calibration error.

We propose to recalibrate and provide a useable PDS archive of these unique data.

Goal 1: We will download, reformat, and re-archive the existing Level-2 data available on the Chinese lunar data system for the PDS in PDS4 format. Our group has several years of experience working with PDS data archiving.

Goal 2: We will develop an instrument model and re-create spacecraft orientations to correct calibration errors in the 3 and 7.8 GHz channels. Where detailed information about the spacecraft structure and state are unavailable, a model will be developed by combining general architectural information that is available with our prior knowledge and the information in the data set itself.

Goal 3: We will archive both the reformatted original Chang'E 2 MRM dataset and our recalibrated data set. All calibration assumptions will be documented and reversible. The recalibrated data set will be provided with clear flagging and labeling of assumptions made.

While the amplitude-dependent studies in Task 1 and 2 will open new windows into the lunar surface composition and rock abundance, the absolute recalibration of the MRM 3- and 7.8-GHz data will allow for new compelling science. Of these, the concept of constraining geothermal heat from orbit, as we will describe in Task 4) is of the most compelling. Even without Task 3, we can produce a relative heat flux map from the Chang'E 3-GHz data that can be compared to ground truth data from Apollo. However, with an absolute calibration we should be able to calculate a constrained thermal gradient independent of ground truth data.

This work will be led by Consultants St. Clair and Million with aid from Science PI Feng and PI Siegler. Goal 1 work will take place predominantly in years 1 and 2, with 0.07 and 0.07 FTE requested for beginning work in year 1 and 0.07 and 0.11 FTE requested in year 2 and 3. The work of Goal 2 will be added into the PDS archived products of the existing Level-2 data in year 3 based on model constraints from Feng and Siegler, but also based on working knowledge of the

spacecraft and Arecibo data which Consultant St. Clair is well versed in. Consultants Million and St. Clair will lead publication of their data processing work.

1.2.5 Task 4: Geothermal heat flux inferred from MRM observations

The Chang'E MRM 3-GHz (and feasibly also the 7.8-GHz) channel receives substantial heat from below the upper meter of the lunar surface. Below ~1m depth, lunar temperatures will increase linearly with depth due to geothermal heat and constant thermal conductivity (Langseth et al., 1976). Instruments such as InSight's HP^3 probe or the Apollo Heat Flow Experiment are designed to dig and measure this gradient. In a low-loss regolith, low frequency microwave data will "see" below the depth of regolith that experiences diurnal temperature variations, probing to the depths where this linear gradient dominates. Therefore, we might expect that the longer wavelength Chang'E data is sensitive to changes in local geothermal heat, at least in areas with low Ti and low rock. As the weighting function is an integration over a given depth range, a small change in the geothermal gradient can have a substantial effect on the brightness temperature, especially in the night. **Figure 13** shows an example of a current fit for 3GHz at low (0%) and high (10%) ilmenite weighting functions, illustrating that a heat flux change of 10 mWm^{-2} should result in a brightness temperature of ~1K. At these depths, ~1m in physical depth for the average lunar loss tangent, the lunar regolith is near its maximum compaction of about 2000 ± 200 kg m^{-3}, meaning that the density (Carrier *et al*., 1991) and therefore thermal conductivity (e.g. Hayne *et al*., 2017) will be fairly uniform and predictable within ~10% error. This allows our constrained geothermal gradient (which is also likely to have errors on the order of 10%) to be converted into a geothermal heat flux within 15-20%, similar to the errors from the Apollo Heat Flow Experiment (Langseth *et al*., 1976).

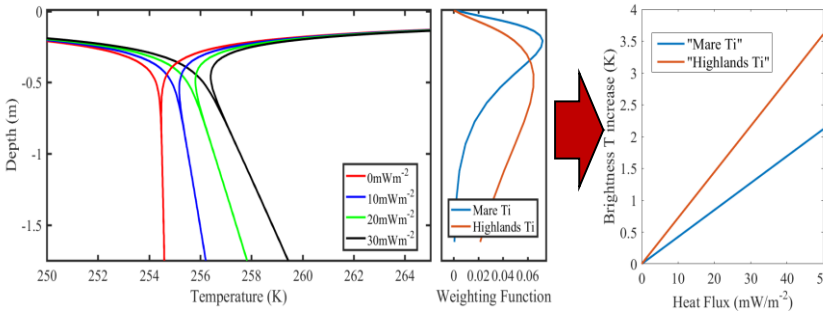

Figure 13: We can calculate Diviner constrained subsurface temperature models for various geothermal heat fluxes (a) and weighting functions (b) to create a model of the increase in midnight brightness temperature as a function of geothermal heat flux (c). Higher T_B means you are seeing deeper or higher heat flux.

Measuring this gradient in a "relative" way, to see if heat flux is higher in one area than another, is likely a reachable goal even without absolute temperature recalibration (Task 3). The MRM data appears to be very repeatable, but simply has absolute offsets. However, an absolute measurement of the geothermal gradient will require the work outlined in Task 3, which is why we have place constraining the geothermal gradient as our 4th and final task. Either a relative or absolute thermal gradient map would be a large leap forward in lunar geophysics,

Radioactive material in the lunar crust is highly heterogeneous, especially on the lunar near side, which is all that we can observe from the ground. Most of the crustal Th, U, and K are concentrated in a single region known at the Procellarum KREEP Terrain (PKT), centered approximately on the Imbrium impact basin. **Figure 14** shows results of a simple global forward model of lunar surface heat flux, which shows higher PKT values. This model assumes GRAIL crustal thickness, LP-GRS (Gamma-Ray Spectrometer) Th concentration [as updated by Warren,

2005] (with U=Th/3.7, K=2500U) uniformly through the crust, a crustal density of 2500 kg m^{-3} and 4mWm^{-2} mantle heat flux.

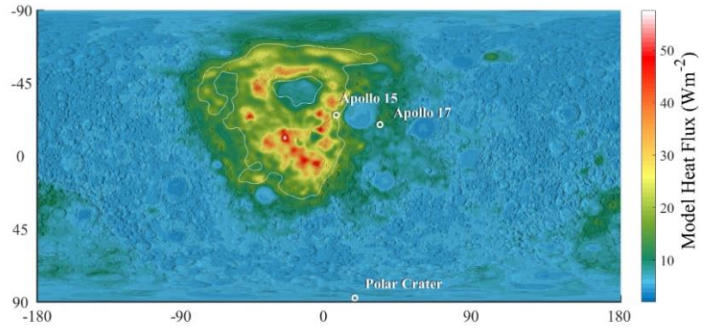

Figure 14: (a) Global forward model of lunar surface heat flux (in mWm^{-2}) assuming GRAIL crustal thickness [Wieczorek *et al.*, 2013], LP-GRS Th [Lawrence *et al.*, 2003] and 4mWm^{-2} mantle heat flux. The large on PKT vs off PKT heat flow difference should be apparent. The white circles mark the Apollo 15 and 17 sites and a recent polar shadowed crater location.

Unfortunately, the anomalous radiogenic concentration in this region was not known before Apollo, not mapped until Lunar Prospector (Feldman *et al.*, 1998; Joliff *et al.*, 2000); both the Apollo 15 and 17 Heat Flow Experiments ([Langseth *et al.*, 1976] the white circles in Figure 13) were located there. This small sample has biased our understanding of the composition of the crust and limited our ability to separate crustal from mantle contributions to lunar heat production (e.g. Siegler and Smrekar, 2014). Global, orbital constraints of geothermal flux by the MRM data, it would vastly improve models of heat production and distribution.

To address this, we build a simple model with an assumed 15m deep lunar regolith (Vasavada *et al.*, 2012) overlying bedrock (3000kg/m^3) with different geothermal heat fluxes. In **Figs. 15a**, we show a model with low-Ti loss tangent (Ti=0%), **Figs. 15b** with a high-Ti model (Ti=12%). Horizontal lines show wavelengths of CE-2 MRM instrument. Dashed lines so diurnal min/max values. We see brightening on the order of ~1K per 10 mWm^{-2} increase in heat flux in low Ti locations (but only about 0.2 K for a 10 mWm^{-2} increase in a high-Ti region).

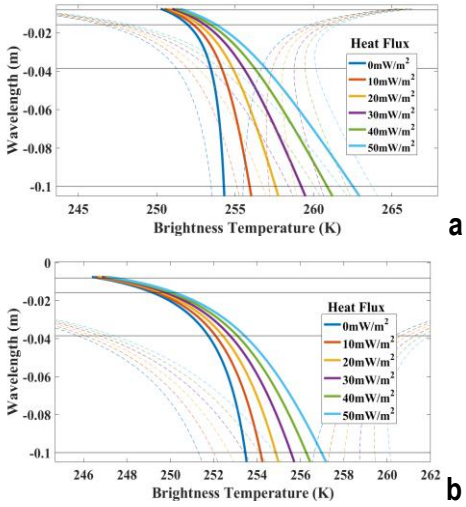

Figure 15: Brightness temperature vs wavelength for different geothermal heat fluxes with an assumed 15m moon-like regolith (a) Low Ti (b) High Ti (12%)

In lieu of longer wavelength data, we can attempt to pull this small signal out of the CE data, but will need to account for Tb variations from latitude, slope, Ti, subsurface rocks, and albedo. **Figure 16** shows the CE-2 3-GHz midnight data corrected for latitude, slope, and albedo variations. This map shows locations where the 3-GHz midnight data is hotter or colder than expected for its latitude and albedo. Note the prominent cooling from high-Ti mare and rocks (e.g., Orientale), but warming of low-Ti areas.

This warm region, elevated by ~3-4 K from the background average is curiously coincident with the region of high thorium seen by the Lunar Prospector GRS instrument (which result in our heat flux model shown as **Figure 14**). In **Fig. 17a**, we take this forward model of geothermal heat flux from **Fig. 14** and our loss tangent (using Clementine spectral Ti) and a simple model including subsurface rocks based on a scaling of Mini-RF CPR [Cahill *et al.*, 2014]. Here we plot the change in T_b from the model average T_b, which should be directly comparable to the CE data shown in **Fig. 16.**

While this model is not yet perfect, it shows a very consistent story that the warming seen in CE data is due to increased geothermal heat flux. To further illustrate this, **Fig. 17b** shows the same forward model, but with a uniform geothermal heat flux, which shows a complete lack of Procellarum region heat.

The fact that the forward model based on our preliminary loss tangent (Feng et al., 2020; Siegler et al., 2020) provides a brightness temperature variation (ΔT_b) similar in magnitude to observed midnight brightness temperatures is very encouraging for this technique. With the models developed in Task 1 and 2, this forward model should become even more reliable than the first order result shown here. Using our absolute recalibration from Task 3, we should be able to change this relative heat constraint into an absolute measure of the geothermal gradient. It may be that the final result of this study is limited due to the penetration depth of the MRM data, but this will feed forward into future instrument design. This work will also be led by Science PI Feng and PI Siegler with efforts (0.5 FTE and 0.08 FTE) divided roughly equally between model fitting of data and working with the processing of the data itself.

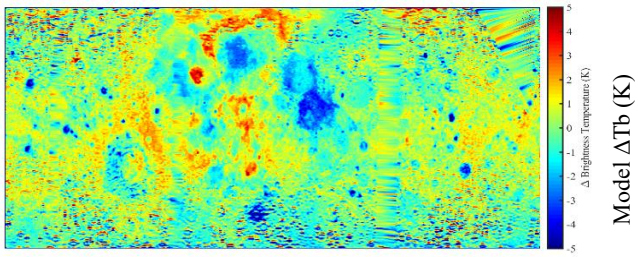

Figure 16: CE-2 MRM 3-GHz midnight data corrected for latitude, slope, and albedo. Note the prominent cooling from high-Ti mare and rocks but residual warming of low-Ti areas in Procellarum.

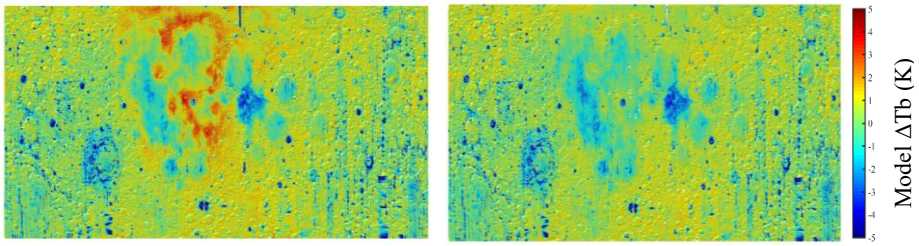

Figure 17: "Δ T_b" from a forward model including Ti, "rocks" scaled by CPR, and (a) geothermal variations as modeled in Fig. 11 and (b) uniform, zero heat flux. Note that the map in (a) resembles Fig. 14 than (b), which appears to be a sign that the Chang'e 3 GHz channel is observing heat flow variations.

1.3 Perceived Impact and Relevance of Proposed Work

Our proposed investigation is integrally aligned with the objectives of the LDAP program. These observations produced significant new data to inform future missions to the Moon and other bodies, but need the analysis described here to be fully utilized. All Diviner data used in this study is currently available on the PDS. The Chang'E data is available in a public PDS-like archive (http://moon.bao.ac.cn/index_en.jsp). The improved one-dimensional thermal model used in this study can be downloaded from https:// doi.org/10.5281/zenodo.3579654 and loss tangent maps are available at https://doi.org/10.5281/ zenodo.3575481. Task 3 will re-archive the original and recalibrated data to the PDS.

This proposed work is directly relevant the objectives of the LDAP which include: "Identification and/or characterization of potential landing sites of high lunar science return (e.g.,...regolith... and compositional properties)" as we are characterizing both surface and subsurface compositional and density anomalies that affect dielectric properties, and "Identification, distribution, transport, and characterization of volatiles in and on the Moon" as microwaves provide a deeper sounding for subsurface ice than has been previously studied. This depth penetration will also aid us in the LDAP goal of: "Identification/characterization of lunar

mineralogy as a function of location and depth" in that we will be able to constrain deep occurrences of ilmenite and/or high-density materials.

This project, models, and instrument design criteria will also feed forward to existing NASA funded projects, primarily a DALI-funded instrument development of a 300 MHz-3 GHz radiometer led by PI Siegler, and an SSO funded mapping of the moon at 470 MHz and 6 GHz by the VLA and Arecibo, also led by the PI, creating a synergy between several programs. The work discussed here is not directly funded by those projects. These related selections highlight NASA's overarching goal to pursue the technology that has currently only been tested in flight by the Chang'E MRM instruments, which have been under-analyzed to date.

2 References and Citations

Bandfield, J. L., Ghent, R. R., Vasavada, A. R., Paige, D. A., Lawrence, S. J., & Robinson, M. S. (2011). Lunar surface rock abundance and regolith fines temperatures derived from LRO Diviner Radiometer data. *Journal of Geophysical Research: Planets, 116*(E12).

Bandfield, J. L., Hayne, P. O., Williams, J.-P., Greenhagen, B. T., & Paige, D. A. (2015). Lunar surface roughness derived from LRO Diviner Radiometer observations. *Icarus, 248*, 357-372.

Bandfield, J. L., Song, E., Hayne, P. O., Brand, B. D., Ghent, R. R., Vasavada, A. R., & Paige, D. A. (2014). Lunar cold spots: Granular flow features and extensive insulating materials surrounding young craters. *Icarus, 231*, 221-231.

Boivin, A., Hickson, D., Tsai, C., Ghent, R., & Daly, M. (2019). *Systematic Broadband Complex Permittivity Measurements of Ilmenite-Bearing Lunar Analog Materials.* Paper presented at the Lunar and Planetary Science Conference.

Cahill, J. T., Thomson, B., Patterson, G. W., Bussey, D. B. J., Neish, C. D., Lopez, N. R., et al. (2014). The miniature radio frequency instrument's (Mini-RF) global observations of Earth's Moon. *Icarus, 243*, 173-190.

Carrier, W. D., Olhoeft, G. R., & Mendell, W. (1991). Physical properties of the lunar surface. In G. Heiken, D. Vaniman, & B. M. French (Eds.), *Lunar Sourcebook* (pp. 475-594). Cambridge, UK: Cambridge University Press.

Elder, C. M., Hayne, P. O., Piqueux, S., Bandfield, J., Williams, J. P., Ghent, R. R., & Paige, D. A. (2016, December). The Lunar Rock Size Frequency Distribution from Diviner Infrared Measurements. In *AGU Fall Meeting Abstracts*.

Fa, W., & Jin, Y.-Q. (2010). A primary analysis of microwave brightness temperature of lunar surface from Chang-E 1 multi-channel radiometer observation and inversion of regolith layer thickness. *Icarus, 207*(2), 605-615.

Feldman, W. C., Maurice, S., Binder, A., Barraclough, B., Elphic, R., & Lawrence, D. (1998). Fluxes of fast and epithermal neutrons from Lunar Prospector: Evidence for water ice at the lunar poles. *Science, 281*(5382), 1496-1500.

Feng, J., Siegler, M. A., & Hayne, P. O. (2020). New Constraints on Thermal and Dielectric Properties of Lunar Regolith from LRO Diviner and CE-2 Microwave Radiometer. *Journal of Geophysical Research: Planets, 125(1), e2019JE006130*.

Feng, J., SU, Y., Liu, J., ZHENG, L., TAN, X., DAI, S., et al. (2013). Data processing and result analysis of CE-2 MRM. *Earth Science (Journal of China University of Geosciences), 38*(4), 898-906.

Gladstone, G. R., Retherford, K. D., Egan, A. F., Kaufmann, D. E., Miles, P. F., Parker, J. W., et al. (2012). Far-ultraviolet reflectance properties of the Moon's permanently shadowed regions. *Journal of Geophysical Research: Planets, 117*(E12).

Gong, X., Paige, D. A., Siegler, M. A., & Jin, Y.-Q. (2014). Inversion of dielectric properties of the lunar regolith media with temperature profiles using chang'e microwave radiometer observations. *Ieee Geoscience and Remote Sensing Letters, 12*(2), 384-388.

Hayne, P. O., Bandfield, J. L., Siegler, M. A., Vasavada, A. R., Ghent, R. R., Williams, J. P., et al. (2017). Global regolith thermophysical properties of the Moon from the Diviner Lunar Radiometer Experiment. *Journal of Geophysical Research: Planets, 122*(12), 2371-2400.

Hu, G.-P., Chan, K. L., Zheng, Y.-C., Tsang, K. T., & Xu, A.-A. (2017). Comparison and evaluation of the Chang'E microwave radiometer data based on theoretical computation of brightness temperatures at the Apollo 15 and 17 sites. *Icarus, 294*, 72-80.

Jolliff, B. L., Gillis, J. J., Haskin, L. A., Korotev, R. L., & Wieczorek, M. A. (2000). Major lunar crustal terranes: Surface expressions and crust- mantle origins. *Journal of Geophysical Research: Planets, 105*(E2), 4197-4216.

Keihm, S., & Langseth Jr, M. (1973). *Surface brightness temperatures at the Apollo 17 heat flow site: Thermal conductivity of the upper 15 cm of regolith.* Paper presented at the Lunar and Planetary Science Conference Proceedings.

Kieffer, H. H. (2013). Thermal model for analysis of Mars infrared mapping. *Journal of Geophysical Research: Planets, 118*(3), 451-470.

Langseth, M. G., Keihm, S. J., & Peters, K. (1976, April). Revised lunar heat-flow values. In *Lunar and Planetary Science Conference Proceedings* (Vol. 7, pp. 3143-3171).

Lawrence, D., Elphic, R., Feldman, W., Prettyman, T., Gasnault, O., & Maurice, S. (2003). Small-area thorium features on the lunar surface. *Journal of Geophysical Research: Planets, 108*(E9).

Lucey, P. G., Blewett, D. T., & Jolliff, B. L. (2000). Lunar iron and titanium abundance algorithms based on final processing of Clementine ultraviolet-visible images. *Journal of Geophysical Research: Planets, 105*(E8), 20297-20305.

Montopoli, M., Di Carlofelice, A., Tognolatti, P., & Marzano, F. S. (2011). Remote sensing of the Moon's subsurface with multifrequency microwave radiometers: A numerical study. *Radio Science, 46*(01), 1-13.

Paige, D., Foote, M., Greenhagen, B., Schofield, J., Calcutt, S., Vasavada, A., et al. (2010). The lunar reconnaissance orbiter diviner lunar radiometer experiment. *Space Science Reviews, 150*(1-4), 125-160.

Paige, D. A. (1992). The thermal stability of near-surface ground ice on Mars. *Nature, 356*(6364), 43.

Sato, H., Robinson, M. S., Lawrence, S. J., Denevi, B. W., Hapke, B., Jolliff, B. L., & Hiesinger, H. (2017). Lunar mare TiO2 abundances estimated from UV/Vis reflectance. *Icarus, 296*, 216-238.

Siegler, M., & Feng, J. (2017). *Microwave Remote Sensing of Lunar Subsurface Temperatures: Reconciling Chang'e MRM and LRO Diviner.* Paper presented at the Lunar and Planetary Science Conference.

Siegler, M., Williams, J., Molaro, J., & Paige, D. (2018). *Temperatures at the Taurus-Littrow Valley: Legacy of the Apollo 17 Heat Flow Experiment and LRO Diviner.* Paper presented at the Lunar and Planetary Science Conference.

Siegler, M., Feng, J., Lucey, P., Hayne, P., Blewett, D., & Cahill, J. (2019). *Deriving the Lunar Loss Tangent and Subsurface Temperatures from the Chang'E-2 MRM and LRO Diviner.* Paper presented at the Lunar and Planetary Science Conference.

Siegler, M., & Smrekar, S. (2014). Lunar heat flow: Regional prospective of the Apollo landing sites. *Journal of Geophysical Research: Planets, 119*(1), 47-63.

Sohn, J.-H., Inaguma, Y., Yoon, S.-O., Itoh, M., Nakamura, T., Yoon, S.-J., & Kim, H.-J. (1994). Microwave dielectric characteristics of ilmenite-type titanates with high Q values. *Japanese journal of applied physics, 33*(9S), 5466.

Ulaby, F. T., Moore, R. K., & Fung, A. K. (1981). Microwave remote sensing: Active and passive. volume 1-microwave remote sensing fundamentals and radiometry.

Vasavada, A. R., Bandfield, J. L., Greenhagen, B. T., Hayne, P. O., Siegler, M. A., Williams, J. P., & Paige, D. A. (2012). Lunar equatorial surface temperatures and regolith properties from the Diviner Lunar Radiometer Experiment. *Journal of Geophysical Research: Planets, 117*(E12).

Vasavada, A. R., Paige, D. A., & Wood, S. E. (1999). Near-surface temperatures on Mercury and the Moon and the stability of polar ice deposits. *Icarus, 141*(2), 179-193.

Wang, Z.-Z., Li, Y., Zhang, X.-H., Jiang, J.-S., Xu, C.-D., Zhang, D.-H., & Zhang, W.-G. (2010). Calibration and brightness temperature algorithm of CE-1 Lunar Microwave Sounder (CELMS). *Science China Earth Sciences, 53*(9), 1392-1406.

Warren, P. H., Ulff-Moller, F., & Kallemeyn, G. W. (2005). "New" lunar meteorites: Impact melt and regolith breccias and large-scale heterogeneities of the upper lunar crust. *Meteoritics & Planetary Science*, *40*(7), 989-1014.

Wieczorek, M. A., Neumann, G. A., Nimmo, F., Kiefer, W. S., Taylor, G. J., Melosh, H. J., et al. (2013). The crust of the Moon as seen by GRAIL. *Science, 339*(6120), 671-675.

Williams, J.-P., Paige, D., Greenhagen, B., & Sefton-Nash, E. (2017). The global surface temperatures of the moon as measured by the diviner lunar radiometer experiment. *Icarus, 283*, 300-325.

Williams, J. P., Greenhagen, B., Paige, D., Schorghofer, N., Sefton-Nash, E., Hayne, P., et al. (2019). Seasonal Polar Temperatures on the Moon. *Journal of Geophysical Research: Planets*.

Woods-Robinson, R., Siegler, M. A., & Paige, D. A. (2019). A Model for the Thermophysical Properties of Lunar Regolith at Low Temperatures. *Journal of Geophysical Research: Planets, 124*(7), 1989-2011.

Zheng, Y.-C., Chan, K. L., Tsang, K. T., Zhu, Y.-C., Hu, G. P., Blewett, D. T., & Neish, C. (2019). Analysis of Chang'E-2 brightness temperature data and production of high spatial resolution microwave maps of the Moon. *Icarus, 319*, 627-644.

3 Data Management Plan

1. Overview of the data that will be produced by the proposed project:

The critical observational data to be produced by this project are (1) georeferenced values corresponding to the loss tangent due to the presence of ilmenite, (2) georeferenced values corresponding to the loss tangent due to surface and sub-surface rocks, (3) georeferenced values corresponding to constraints on the geothermal heat flux as measured from orbit, and (4) recalibrated and corrected 3 and 7.8 GHz data based on model outputs. The derived observational data described above will be either partially or completely outputs of models that will be instantiated as software source code. Additional software tools or scripts will also be produced to validate the data or derive specific results for publication. Any data or source code that underlies published results (for which "publication" may include, but not be limited to, conference presentations, peer-reviewed journal articles, or PDS archiving) will be made publicly available by the end of the project. The intention is that any substantive result should be fully replicable using only public domain information and without additional input from this project team.

2. Data types, volume, formats, and (where relevant) standards:

Most of the primary and secondary data products listed above will be structured as tabulated or non-tabulated ASCII. The attached letter of support from GEO establishes a commitment to work with this project to produce data that is compliant with PDS requirements and ingest and support those data at no cost to this project. We estimate that the total volume of data produced by this project---including primary observational and derived data, documentation, metadata, scripts, data underlying published results, and software---will be less than 100 MB. Documented source code will be included in PDS bundles "as documentation" when permitted, and all relevant source code will be published to an appropriate public repository (the NASA PDS Github if possible) by the end of the project.

3. Schedule for data archiving and sharing:

The preparation for archiving data in the PDS will begin as soon as the first reprocessed data becomes available in the last half of YR1 and continue throughout the project as new data sets become available. Data bundles will be submitted to the PDS no later than the first half of YR3, and possibly sooner, for reviewing and archiving. Source code documentation and cleanup will likewise be ongoing, with release of source code to occur no later than the end of the project or along with a significant publication, if appropriate for reproducibility.

4. Intended repositories for archived data and mechanisms for public access and distribution:

The project team is committed to open and reproducible research and to the creation of high-quality and well-documented data products for reuse by the community. All data and metadata will be formatted according to Planetary Data System (PDS) standards. The attached letter of support from GEO node of the PDS establishes a commitment to work with this project to produce data that is compliant with PDS requirements and ingest and support those data at no cost to this project. All data archived in the PDS is considered "in the public domain" and made available without restriction. When this award results in peer reviewed publications, the data behind any published figures, tables, maps or results will be made available electronically at the

time of publication. When possible, such data will be included as supplements to the papers themselves. Such data will be published to Github or an appropriate online public data repository. When appropriate, such data will also be archived in the PDS by the end of the project.

5. Plan for enabling long-term preservation of the data:

The PDS is the primary long-term archive for NASA-supported planetary data. The planned preservation horizon for data archived in the PDS is not less than 50 years.

6. Software archiving plan:

All source code, scripts, other executable digital data, and attendant documentation created under this award will be retained in the PI's records. When legal and feasible, source code for software created under this award will be published to the NASA Planetary Science Github by the end of this project. Where such software is critical to the results of research performed under this award, source code will be accompanied by documentation describing the hardware / software operating environment in which the software was developed and used, including external software dependencies and libraries and descriptions of tests or scripts that, at minimum, reproduce the results upon which any published research relies. When legal and feasible, virtual machine images (e.g. VirtualBox) or software containers (e.g. Docker, Singularity) that instantiate running examples of such software will be published to an appropriate public data repository (e.g. Zenodo). When this is not feasible---for example, due to restrictive licensing of dependencies---the containers or images will be created and preserved in the PI's records.

7. Astromaterials archiving plan:

The project will not involve acquisition of collection of astromaterials.

8. Roles and responsibilities of team members for data management:

Preparation of data and software for archiving or other preservation will be performed by Chase Million and Michael St. Clair of Million Concepts LLC. These tasks include: (1) cleanup and documentation of data, (2) cleanup and documentation of source code, including documenting the operating environment and creating or documenting unit or regression tests, (3) preparing metadata and documentation according to PDS4 standards, and (4) submitting properly prepared data to PDS for review and responding to any required liens until the data are accepted into the archive. Million and St. Clair have significant prior experience with data and software archiving and preservation, including preparing and submitting data for archive under the PDS4 standard.